Photo-Activated Phosphorescence of Ultrafine ZnS:Mn Quantum Dots: on the Lattice Strain Contribution

Antonio Valerio Longo [a,b*], Baptiste Notebaert [a,b], Mériem Gaceur [b] , Gilles Patriarche [c], Alice Sciortino [d], Marco Cannas [d], Fabrizio Messina [d], Hans Jurgen von Bardeleben [e], Nicolas Battaglini [a], and Souad Ammar [a*]

[a]Université de Paris, CNRS UMR-7086, ITODYS, 15 rue Jean-Antoine de Baïf, 75205 Paris, France
[b]ACTINOVA SAS, 571 Route de Molières, 82440 Mirabel, France
[c]Université Paris Saclay, CNRS UMR-9001, C2N, 10 Boulevard Thomas Gobert, 91120 Palaiseau, France
[d]Dipartimento di Fisica e Chimica "Emilio Segré", Università degli Studi di Palermo, Via Archirafi 36, 90123 Palermo, Italy
[e]Sorbonne Université, Campus Pierre et Marie Curie, Institut des Nanosciences de Paris, 4, place Jussieu, 75005 Paris, France
*e-mail addresses: antonio.longo@univ-paris-diderot.fr, ammarmer@univ-paris-diderot.fr,

ABSTRACT

We address the enhancement of orange-light luminescence of Mn-doped Zinc sulfide nanoparticles (NPs) induced by exposure to UV light. Ultrafine ZnS:Mn NPs are prepared by microwave-assisted crystal growth in ethanol, without adding any dispersant agents. When exposed to UV light, their orange emission intensity undergoes a strong increase. This effect is observed when the NPs are deposited as a thin layer on a transparent substrate, or dispersed in a ethanolic suspension. Such a feature was already observed on polymer- or surfactant-coated ZnS:Mn NPs and explained as a passivation effect. In this study, by coupling X-ray photoelectron, Fourier transform infrared and electron paramagnetic resonance spectroscopy, we establish that this photo-activated luminescence is rather the consequence of lattice-strain effects. Indeed, our data show that UV irradiation in air promotes surface oxidation, replacing the outer sulfide layer with a sulfate one. The mismatch between the resulting outer crystallographic metal sulfate lattice and the inner sulfide one induces mechanical strains on the latter, thus partially relaxing the selection rules controlling the formally spin-forbidden electronic transition from the $^4T_1$ to the $^6A_1$ molecular states of the $[MnS_4]^{6-}$ emitting centers. These results are relevant because they shed light on the long controversial discussions on the origin of the photo-activated phosphorescence in such systems.

INTRODUCTION

II-VI semiconducting nanocrystals have attracted considerable attention due to their quantum confinement effect, which provides a route to tailor their electronic and optical properties by varying the size [1] . Among them, Zinc sulfide nanoparticles (NPs) [2] are widely used due to their weak toxicity [3,4] compared to cadmium or mercury chalcogenides. They are typically employed in displays, optical-based sensors and lasers [2,5,6]. Their optical response may be also varied by doping them [7–12], the introduced impurities acting as emitting centers within their quantum-confined crystalline structure. In these cases, the excitation is transferred from excited states (such as excitonic or surface ones) to the dopant states, in competition with the dominant recombination mechanism [13–15]. Manganese is certainly one of the most common

dopants in ZnS. As a divalent cation, it occupies substitutional zinc sites in the ZnS blende lattice, and its excitation and decay, within this hosting matrix, produce an orange luminescence at a wavelength of approximately 580-590 nm. This emission peak is generally ascribed to the formally spin-forbidden electronic transition between $^4T_1$ and $^6A_1$ energy levels of tetrahedral $[MnS_4]^{6-}$ molecular species [8]. The transition between these two states is formally forbidden because of the violation of two selection rules, namely the one associated to the spin ($\Delta S = 0$) and the Laporte rule associated to the orbital quantum number L ($\Delta L = \pm 1$). The former is partially lifted by the spin-orbit interaction, the latter by the coupling with the crystal host. As a matter of fact, since the wavefunctions must reflect the symmetry properties of the host, the absence of inversion symmetry in a tetrahedral scenario induces a hybridization of p and d orbitals of Mn, resulting in a lifting of orbital selection rules.

A huge number of works exist on the preparation and the optical characterization of ZnS:Mn NPs [16–18] as well as on the closely-related ZnS@ZnS:Mn core-shell nanosystems [19,20]. Some of these works pointed out the characteristic irradiation-induced enhancement of the typical orange photoluminescence, which is observed independently of the surface features of the studied particles. Indeed, Bol et al. observed that the orange emission intensity increases with the UV irradiation time for polymer-coated ZnS:Mn NPs. They attributed such a feature to some surface-passivation effects, the adsorbed species being cured by the UV light [19,20]. Cruz et al. [20,21] reported the same feature on acrylic-acid-coated ZnS:Mn NPs. They also incriminated UV curing, the photochemical reactions on adsorbed acrylic acid monomers leading to a coating of the exposed NPs by a passivation polymeric layer. Cao et al. also reported the increase of orange-emission intensity of Mn centers with respect to UV irradiation time in ZnS:Mn NPs, prepared in the presence of dioctyl sulfosuccinate surfactants [23]. They invoked a surface passivation effect as a consequence of UV curing of the residual dioctyl sulfoccinate ligands. Thai et al. [24] investigated the same phenomenon on hydrothermally-prepared NPs in the presence of thioglycolic acid, which by thermal decomposition provides the required sulfide ions for metal sulfide precipitation and glycolic acid moieties, of which hydroxyl groups coordinate the particle surface during the particle growth. They supposed that UV irradiation favors a surface photochemical process, for which a change of the α-hydroxyl acetic acid creates surface passive polymeric shells able to prevent non-radiative recombination. They did not exclude the possibility of dioxygen molecules, adsorbed directly onto the particle upper surface, reacting with redundant S and Zn atoms to form a passivation sulfate layer. This mechanism was specifically retained by Dunstan et al. to explain the photo-activated phosphorescence wet-prepared surface-free ZnS:Mn NPs [25]. They suggested the same photocorrosion process, during which species like SO_4^{2-}, SO_3^{2-}, and S were produced on the NP surface, acting as surface e^-/h^+ recombination centers. Within the same idea, Jung et al. [26] voluntary promoted surface oxidation of ZnS:Mn NPs by UV irradiation with oxygen bubbling and compared their optical properties to their pristine counterparts. They reported a quantum-efficiency increase on the treated particles and attributed the observed phosphorescence improvement under prolongated UV excitation (several hours) to the same photocorrosion surface passivation with the formation of a zinc

sulfate outer layer. UV photoactivation of manganese emission was also observed on polymer-free ZnS-coated CdS:Mn nanocrystals, with the *in situ* formed $ZnSO_4$ outer layer claimed to be at the origin of a strong passivation effect.

In almost all these studies, it is reported an intensity increase of the whole photoluminescence spectra. In other words, the intensity of both the broad blue/green emission around 450 nm, which is also observed in undoped nanocrystalline ZnS NPs and usually ascribed to a defect-related emission of surface blende lattice, and the orange emission around 580 nm, attributed to the spin forbidden $[MnS_4]^{6-}$ transition, increases after UV irradiation [19–24]. Moreover, in these same works, the relative intensity increase of the former appeared to be stronger [19,20]. These results support the passivation mechanism of surface states, that strongly increases the relative contribution of radiative recombination of the delocalized charge carriers by countering that effect of trapping surface states. In the case of orange emission, once the excitation energy is localized on the Mn^{2+} centers in their excited state, surface passivation is less important. Noteworthy, this comparative analysis of the collected intensity between the ZnS defect and the Mn^{2+} related emissions fails for certain types of particles, typically those with a surface free from any coating. Indeed, in these cases only the orange-emission intensity appeared to be affected.

In this work we chose a microwave-assisted synthesis route allowing to prepare ultrafine blende ZnS:Mn nanocrystals to enhance all the surface effects. Microwave-assisted synthesis techniques have proved to be a facile and efficient way to tailor the size of obtained NPs[27-30]. Our specific synthesis route consists of a sulfidation reaction of zinc and manganese acetate salts (within the nominal 0.98:0.02 atomic ratio) in ethanol (bp ~ 60°C) using thioacetamide as a sulfide source. Indeed, at a so low and short temperature and time reaction, metal sulfide nucleation would predominate against crystal growth diffusion leading to very small particles. Moreover, operating in the absence of any dispersing agents, like surfactants or polymers, favors the production of particle surfaces free from organic coating, making the previously discussed passivation mechanism under UV irradiation potentially less significant. In this way we should maximize the number of surface-defect states and localize a maximum of the manganese emitting centers on the surface of the engineered nano-objects.

So, besides an advanced study of the optical properties of the produced particles in order to highlight their photo-activated phosphorescence, a battery of structural characterization studies was carried out so as to well describe their volume and surface structures using local analysis techniques, like X-ray Photoelectron Spectroscopy (XPS), Fourier Transform InfraRed spectroscopy (FTIR), Electron Paramagnetic Resonance spectrometry (EPR) and High Resolution Transmission Electron Microscopy (HR-TEM), as well as macroscopic ones, like X-Ray Diffraction (XRD). The collected data are discussed hereafter and used to clarify the elusive origin of the UV-induced photoluminescence enhancement. Interestingly, we find that UV irradiation in air promotes surface oxidation replacing the outer metal sulfide layer with a sulfate one. Rather than a passivation effect, we assert that this outer layer induces local strains on the emitting $[MnS_4]^{6-}$ centers, thus partially lifting the selection rules associated with the formally spin-forbidden transition between the $^4T_1$ and $^6A_1$ molecular

states. The idea of strain effects on the phosphorescence enhancement of ZnS:Mn particles was already suspected, although less highlighted compared to passivation effect, by Thai et al. [24]. These authors also reported a photoluminescence-intensity increase over UV irradiation time on their particles synthesized from thioglycolic acid $HSCH_2CO_2H$ and initial chemicals $Zn(CH_3CO_2)_2.2H_2O$, $Mn(CH_3CO_2)_2.4H_2O$ by the hydrothermal method. Interestingly, differently from all previous studies, they found that the increase of the yellow-orange emission intensity was stronger than that of the blue-green one [24].

METHODS

Chemicals. Zinc(II) acetate, manganese(II) acetate (Sigma-Aldrich, 99.9 %), thioacetamide (Sigma-Aldrich, ≥ 99 %) and absolute ethanol (VWR, > 99.5 %), were purchased and used as received.

Particle Synthesis. Manganese-doped ZnS NPs were synthesized through a *chimie douce* route. It consists of a microwave-assisted ethanol process, dissolving zinc and manganese acetates (889 mg and 24 mg, respectively) and thioacetamide (373 mg) as sulfur source in ethanol (20 mL). Thioacetamide decomposition, sulfidation and condensation reactions proceeded by heated the resulting solution in a multiwave Anton Paar microwave oven for 25 minutes under a constant radiation power of 220 W. The produced particles were then recovered by centrifugation, washed in ethanol and then dried in air.

Particle characterization. The crystalline structure of the prepared particles was checked by XRD using a X'pert Pro diffractometer (Panalytical, Almelo, Netherlands), equipped with a Co Kα X-ray tube (40 kV and 40 mA) and working in the Bragg-Brentano θ-θ reflection geometry. A ω-2θ (ω = 1°) grazing incidence configuration was applied to evidence any structural changes on these particles after UV irradiation, replacing the former diffractometer by an Empyrean one (Panalytical), equipped with a Cu Kα X-ray tube (40 kV and 40 mA) and a five-axes cradle with motorized movements for sample positioning. In practice, the particles were dispersed in ethanol and exposed to UV light (305 nm) for 30 minutes before to be deposited on a ITO/glass substrate by spin coating. The XRD pattern of the resulting film was recorded, as well that of the fresh film. All the collected data were then analyzed by HighScore (version 5.1, Panalytical, Almelo, Netherlands) and MAUD (version 2.55, Trento, Italy) software. The morphology of the particles was also checked by transmission and scanning transmission electron microscopy (TEM and STEM), working in bright field (BF) or high-angle annular dark-field imaging (HAADF) modes on a FEI TITAN 200 microscope, operating at 200 keV. Once again, the observations were achieved on fresh particles and irradiated ones, using the same colloidal ethanolic solutions than previously. To complete these analyses, XRF and XPS spectroscopies were performed, before and after UV irradiation, to quantify the chemical composition of the produced particles in volume and surface, respectively. A MINIPAL4 XRF spectrometer (Panalytical, Almelo, Netherlands),

equipped with a rhodium X-ray tube (30 kV and 87 μA) and a K-Alpha+ XPS spectrometer (ThermoFisher Scientific, East-Grinstead, UK) equipped with a micro-focused and monochromatic Al Kα X-ray source (1486.6 eV, spot size of 500 μm) were used. XRF quantification was achieved thanks to Zn, S and Mn standard solutions. XPS quantification was performed by first calibrating the recorded spectra against the (C—C/C—H) C 1s component set at 285 eV and by using the manufacturer sensitivity factors thanks to the Avantage software (version 5.9902, East-Grinstead, UK). Survey spectra to identify elements were collected in steps of 1 eV at pass energy of 100 eV. High-resolution ones of separate photoelectron lines (C, O, S, Zn, Mn) were taken by steps of 0.1 eV at pass energy of 40 eV. This series of characterizations was completed by IR spectroscopy (KBr method) using a FT-IR spectrophotometer model 1750 (Perkin-Elmer, Wellesley, USA) operating in the transmittance mode between 4000 and 500 cm^{-1}. Finally, EPR measurements were performed with a standard X-band (9 GHz) spectrometer at room temperature (300 K). The spectra were recorded at 0 to 6 kOe, on the fresh and UV-exposed films, replacing just glass substrates by quartz ones, and they were recorded on fresh and UV-illuminated (1 hour at 365 nm) powders, recovered by centrifugation of the previous ethanolic colloids, and placed in quartz tube (~10 mg).

Optical studies were carried out by plotting both the absorption and emission spectra of the recovered particles, dispersed in ethanol as relatively stable colloids or deposited on a quartz substrate as more or less continuous thin films. Absorption spectroscopy measurements were carried out using a UV–Visible–NIR spectrometer, model Cary 56E (Agilent, Santa Clara, USA), operating in both transmission and diffuse reflectance modes within the 290-800 nm spectral range. Emission spectroscopy was carried out in solution using a FluoroMax-4 spectrofluorometer (Horiba Jobin Ivon, Kyoto, Japan). Additionally, time-resolved photoluminescence measurements were recorded, on colloidal samples exclusively, using an intensified, time-gated charge-coupled device (CCD) camera, while exciting the sample via a tunable laser system, which consists of an optical parametric oscillator pumped by a Q-switched Nd:YAG laser (5 ns pulses at 10 Hz repetition rate, ~ 150 μJ/pulse. The spectral resolution of the setup was equal to 4 nm. The CCD camera records the sample emission spectrum at a certain delay from the laser pulse and for a fixed time window of 0.5 ns; the spectral evolution can then be obtained by repeating the measurements at different delays.

RESULTS AND DISCUSSION

Synthesis of Mn-doped ZnS NPs

The synthesis protocol employed in this work consists of microwave-assisted sulfidation reaction of zinc and manganese acetate salts (within the nominal 0.98:0.02 atomic ratio) in using thioacetamide as a sulfide source. Sulfidation reaction proceeds through thioacetamide decomposition. At the solid state, this decomposition occurs at a temperature higher than

thioacetamide melting (114°C), leading to acetonitrile CH_3CN and hydrogen sulfide H_2S, which serves as sulfide source. In solution, the decomposition occurs at a lower temperature and two routes are possible: i) the hydrolysis reaction in the presence of water [31] (Eq. 1-3) and (ii) the direct reaction [32–34], taking advantage of thioacetamide chelating properties [32] (Eq. 4):

$CH_3(CS)NH_2 + H_2O \rightarrow CH_3(CO)NH_2 + H_2S$ Eq. 1

$H_2S \rightarrow S^{2-} + 2H^+$ Eq. 2

$S^{2-} + M^{2+} \rightarrow MS$ Eq. 3

$M[CH_3(CS)NH_2)]_2 = MS + H_2 + CH_3CN$ Eq. 4

In polar solvents [31,35,36], the former mechanism predominates above 50°C, the metal sulfide precipitation rate increasing when the temperature increases. Microwave-assisted ethanol process may benefit from it favorizing precipitation of ultra-small metal sulfide crystals.
This was first confirmed by XRD analysis of the recovered particles (Fig. 1). The recorded pattern matches very well the blende zinc sulfide structure (ICDD n°98-006-7790). A successful refinement was performed with a crystal size ranging between 25 and 30 Å.

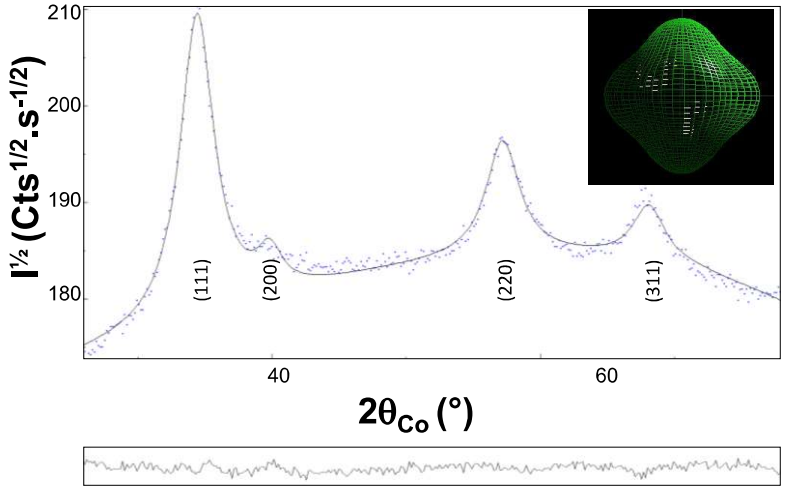

Figure 1. Experimental (scatter) and calculated (blue line) XRD patterns of the freshly-produced particles. The residue, defined as the difference between the experimental and calculated diffractograms, is given in the bottom to illustrate the fit quality (Bragg reliability factor of 2.7). A pseudo-Voigt function was used for modelling the peak profile while the atomic coordinates of all the atoms in the blende lattice were fixed as well as their occupation site ratios in relation to the nominal chemical composition. In the inset, the Rietveld-inferred representation of the coherent crystallographic domains is given for information.

Transmission and scanning transmission electron microscopy (TEM and STEM), operating in Bright Field (BF) and High-Angle Annular Dark-Field imaging (HAADF) modes, respectively, were performed and confirm that the produced particles crystallized in blende structure as shown by their electron diffraction pattern (Fig. 2). A statistical analysis of the size distribution of the observe NPs (see Fig. 2d) gives an average size of 3.5 nm. Note that this size is close to the Bohr radius, so that a quantum confinement effect is expected [37]. Moreover, for such an average size, the surface per volume atomic fraction statistically

exceeds 30% [38], meaning that a large fraction of manganese atoms will be on the particle surface, sensitive to any surface change.
Elemental mapping confirmed chemical homogeneity of the NPs under examination (see Fig. S1 in the supporting information) and their X-ray Energy dispersive spectra quantified their real Mn content, which was found to be very close to the nominal 2 at.-% value. These results were corroborated by X-Ray Fluorescence spectroscopy (XRF) and XPS.

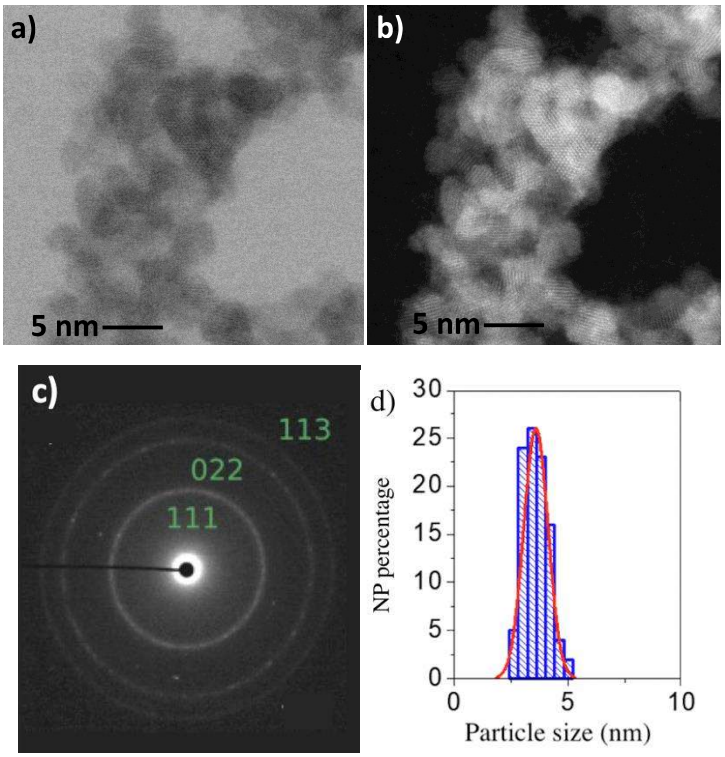

Figure 2. a) TEM-BF and b) STEM-HAADF images of an assembly of ZnS:Mn particles and their c) electron diffraction patterns, fully indexed within the blende structure. d) Size distribution of the observe NPs. The Gaussian fit (red line) peaks at 3.5 nm and has a FWHM of 1.3 nm.

XPS provided us additional information. Indeed, the high resolution Zn_{2p}, Mn_{2p} and S_{2p} spectra are in good agreement with the expected Mn-doped ZnS blende phase. The measured binding energies, 1022.0, 1046.0, 161.7 and 162.5 eV of the of the $Zn_{2p3/2}$, $Zn_{2p1/2}$ $S_{2p3/2}$ and $S_{2p1/2}$ peaks, respectively (Fig. 3) correspond fairly to those of the ZnS blende nanostructures and are very close to those already reported in the relevant literature [39–42]. Besides, we see a clear signature of the $Mn_{2p3/2}$ and Mn_{3p} signals, even though weak in intensity, at binding energies (641.1 and 49.6 eV, respectively) characteristic of Mn^{2+} cations [43–45], confirming manganese ZnS doping. Note that, compared to the the Mn_{2p} line, the Mn_{3p} one is usually assumed to be less sensitive to the bonding environment of manganese [E. S. Ilton, J. E. Post, P. J. Heaney, F. T. Ling, S. N. Kerisit, Appl. Surf. Sci. 366, 2016, 475–485] [R. P. Gupta and S. K. Sen, Phys. Rev. B 10(1), 1974, 71-77]. As a consequence it is seldom analyzed to characterize manganese –based inorganic solids. For our purpose, its evidence in the XPS

spectrum of the as-produced NPs confirms their Mn^{2+} doping (the high signal to noise ratio in this binding energy area forces us to limit our analysis to a simple qualitative description of the spectrum, tacking in mind that relaxation phenomena may proceed between the 3p and the unsaturated 3d manganese energy levels, during the photo-ionization process, contributing to the peak broadening).

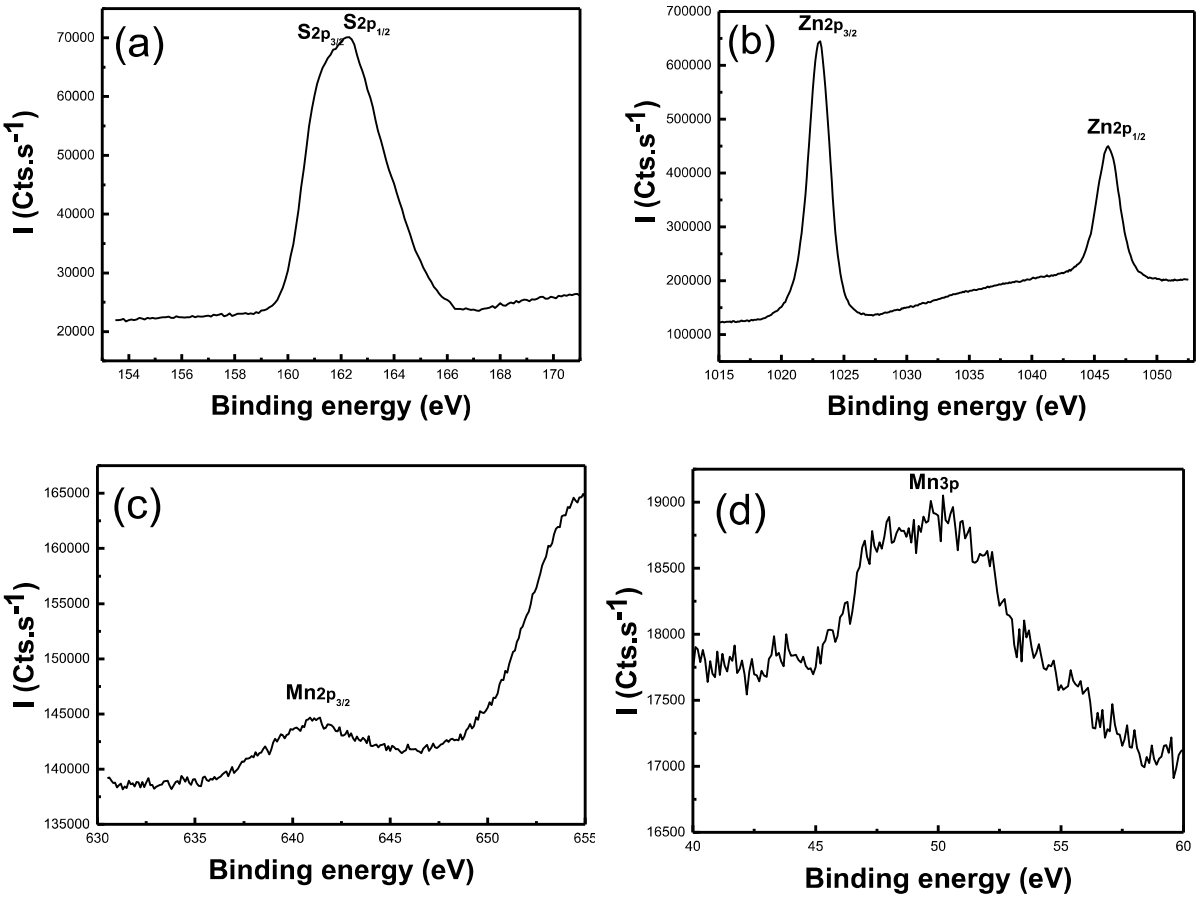

Figure 3. High Resolution XPS spectra pf the (a) S_{2p}, (b) Zn_{2p}, (c) Mn_{2p} and (d) Mn_{3p} signals recorded on the freshly-prepared ZnS:Mn particles by the ethanol microwave route. Peak fitting was specifically performed on sulfur signal to deconvoluate it into $2p_{3/2}$ and $2p_{1/2}$ contributions (see Fig. S2 in the supporting information section). It was not carried out on manganese and zinc 2p signals since their own spin-orbit splitting is already well resolved (~11 [B. R. Strohmeier and D. M. Hercules J. Phys. Chem. 88(21), 1994, 4922-4929] and ~23 eV, [B. R. Strohmeier and D. M. Hercules, J. Catal. 86, 1984, 266-279] respectively).

We now focus on the optical characterization of the as-produced particles By recording their absorption and fluorescence optical spectra in ethanolic colloidal dispersion. They display a strong absorption band around 285 nm, related to the band-to-band transition of their constituting semiconducting crystals (Fig. 4). This value, corresponding to a photon energy of 4.35 eV, is higher than the typical one for a bulk crystal. The Tauc plots (Fig. S2 in the supporting information) obtained from absorption data allow us to estimate a bandgap around 4.05 eV, higher than the reported value of 3.54 eV for bulk cubic ZnS, confirming the

anticipated quantum-confinement effect. In parallel, the photoluminescence spectra exhibit three main peaks, one in the UV region (around 310 nm), due to band-to-band recombination, another around 420 nm, usually attributed to zinc vacancies in the crystalline structure [2,7] and a third at 590 nm attributed to the spin-forbidden $^4T_1$–$^6A_1$ transition of the $[MnS_4]^{6-}$ centers [7]. The spin-forbidden nature of the latter makes difficult to excite this transition directly with a simple spectrophotometer lamp. On the contrary, it is possible to observe it by exciting the sample in the UV region. This behavior has been confirmed by a PhotoLuminescence Excitation (PLE) measurement (not shown).
The attributions mentioned above were confirmed by time-resolved spectroscopy, showing that the peak at 310 nm exhibits a mono-exponential decay kinetics with very short lifetimes ranging around 3 ns. The one at 420 nm presents an almost mono-exponential decay kinetics with lifetime time close to 1.6 ns, with a small fraction (around 4%) of fluorophores exhibiting a slower decay time (Fig. S3 in the supporting information).

On the contrary, the band at 590 nm presents a much slower and complex behavior, with the decay kinetics reasonably fitted by a stretched exponential decay (Fig. 4c). The latter is described by the following expression, with the dimensionless stretching parameter β varying between 0 and 1:

$$y = \exp\left[-\left(\frac{t}{\tau}\right)^{\beta}\right]$$

The physical meaning of such a behavior lies in the fact that inside the choromophores population a distribution of the excited-state lifetimes exists around a mean value τ. In particular, we found a mean value τ around 70 μs, and a value β around 0.4. Now, the lower is the value of the β parameter, the larger is the distribution of the lifetimes around τ (so that for β = 1 the monoexponential decay is recovered). The case of β = 0.4 corresponds to a very broad distribution, for which it is possible that a small part of the chromophore population has an excited-state lifetime which can be many tens of times larger than the mean one τ. To give a quantitative view of the increasingly slower decay due to the stretched (β = 0.4) behavior, we observe that while for t = τ the initial intensity value is reduced by a factor 1/e (this is true for any value of β), a $1/e^2$ and a $1/e^3$ reductions are observed after a time 430 μs and 1.51 ms, respectively, in marked contrast with a monoexponential decay, for which the same reductions are obtained after 2τ = 160 μs and 3τ = 240 μs, respectively. If all the manganese centers were identical, a monoexponential decay would be expected. Clearly this is not the case, indicating that an effect able to locally modify the optical properties of the emitting centers must be present. As discussed more in detail below, this observation is coherent with an effect due to a local lattice strain around the emitting centers.

Effect of UV irradiation

The effect of UV irradiation on the emission spectra of the ZnS:Mn has been addressed, focusing on their ethanolic colloidal dispersion. In particular, the intensity of the orange

emission is relatively low in the as-grown sample, but is observed to quickly grow under UV illumination. In Fig. 5, the effect of UV irradiation is reported under different conditions.

Fig. 5a shows a selection of emission spectra collected *in situ*, under prolonged exposure to a laser radiation having wavelength 310 nm. We show an increase of the orange emission intensity over time *t*, while the blue emission intensity remains negligible. The relative detailed kinetics is shown in Fig. 5b. We want to stress that the described effects are permanent.

As a point of reference, an enhancement of the orange emission of a factor around 3.5 is observed over a period of 2000 s under illumination (Fig. 5b). This phosphorescence intensity increase was also visually observed on thin films of NP obtained by spin-coating process from freshly prepared ethanolic ZnS:Mn dispersion on ITO/glass substrates and subsequently exposed to a 305 nm UV lamp (see Fig. S4 in the supporting information).

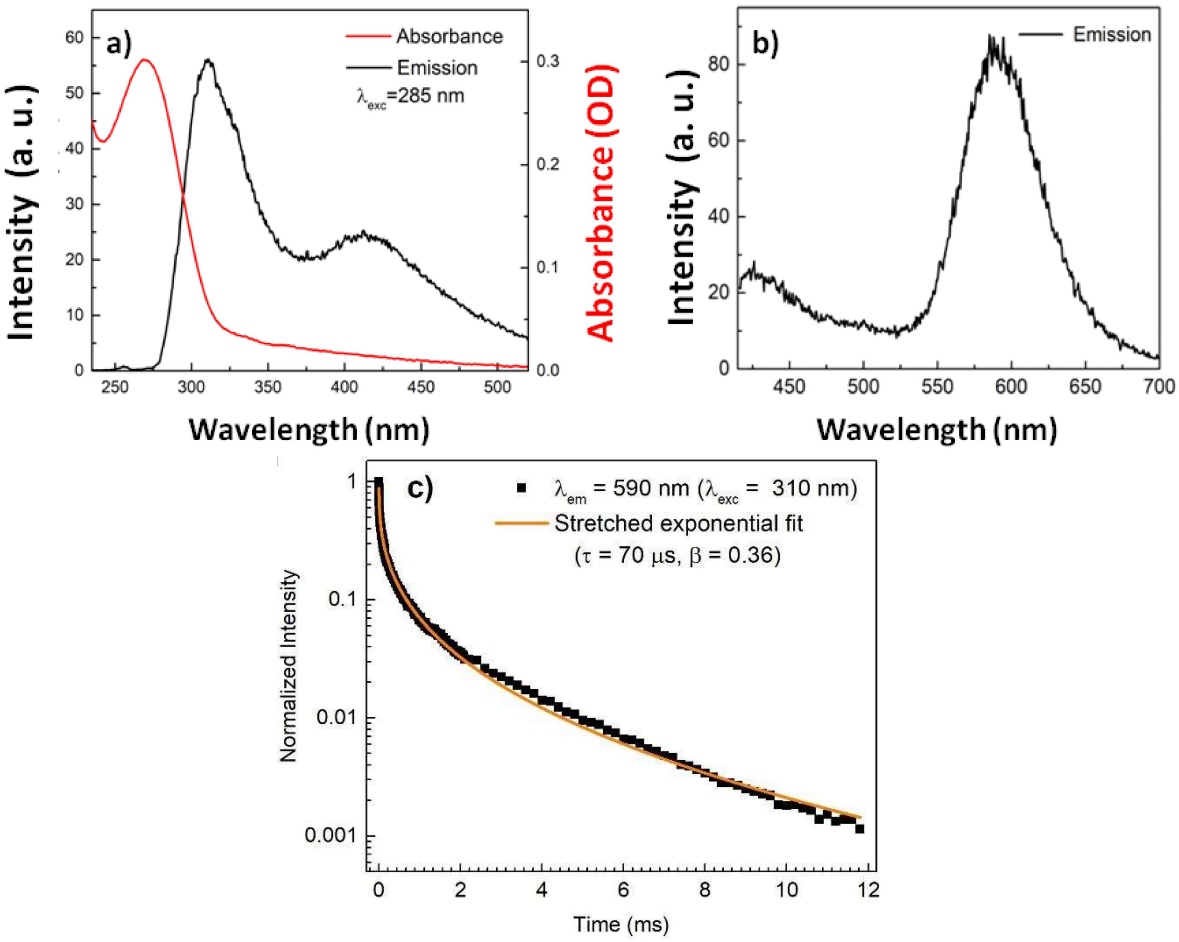

Figure 4. a) UV-Visible absorption (red line) and emission (black) spectra recorded, within the 220-540 nm wavelength region, on a colloidal dispersion in ethanol of the produced particles. b) Emission spectrum of the same suspension recorded in the 420-700 nm wavelength region. The main emission peak at 580-590 nm highlights the orange-colored luminescence of the colloidal dispersion. c) Decay kinetics of the phosphorescence transition associated with the $[MnS_4]^{6-}$ emitting centers.

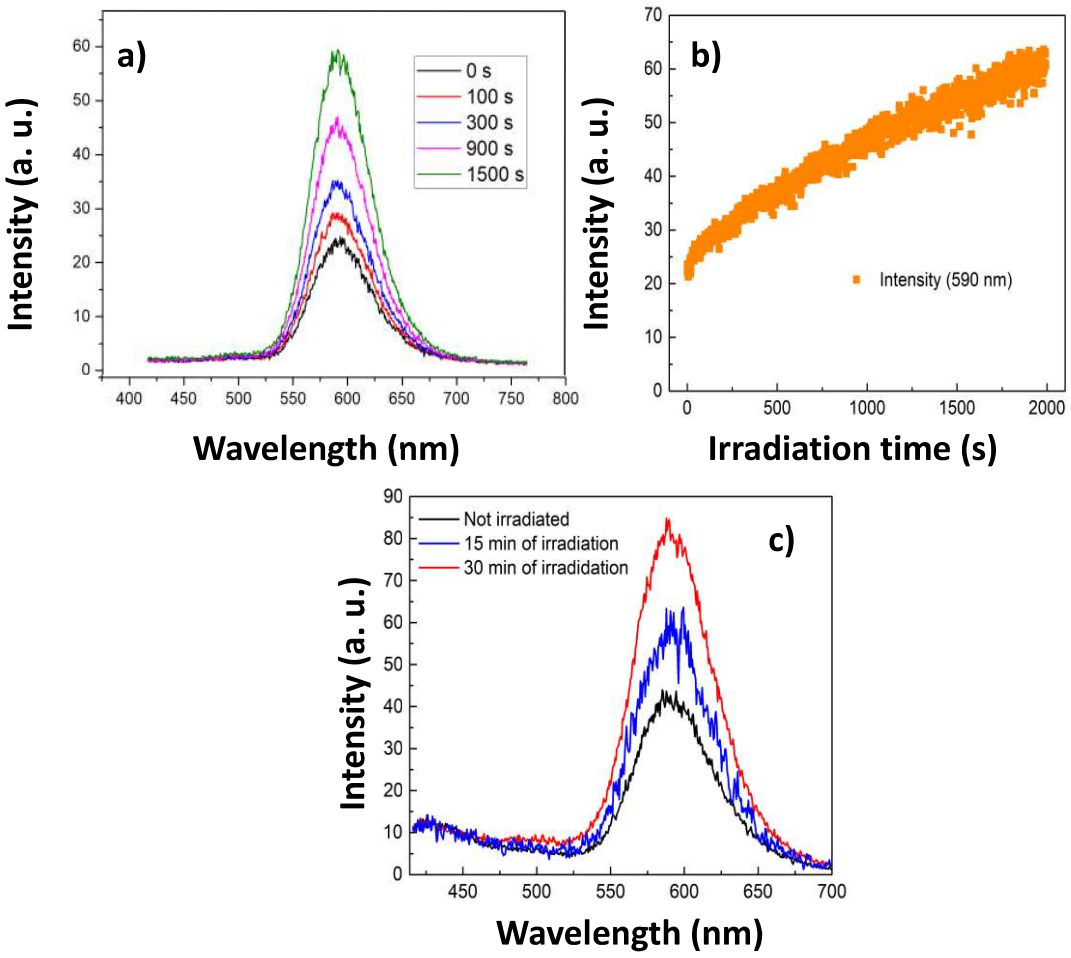

Figure 5. a) Visible emission spectra collected on a concentrated core-shell particle suspension for different UV irradiation times ranging from 0 to 1500 s ($\lambda_{excitation}$ = 310 nm). b) Orange emission band intensity variation over a continuous UV irradiation time, consistent with a monotonic non-exponential time dependence. c) Visible emission spectra collected on a diluted ethanolic suspension for different UV irradiation times ranging from 0 to 1800 s ($\lambda_{excitation}$ = 310 nm).

Figure 5c shows the effect of UV irradiation on a solution having a concentration 5 times lower with respect to the one associated with Fig. 5a. We highlight that the concentration has an effect on the emission linked to Zn defects (the one peaking around 420 nm), which becomes more intense at lower concentrations. This allows us to remark how this optical activity is unaffected by prolonged emission to UV light. In fact, the intensity of this blue emission is found to be insensitive to the irradiation time, very differently from what is observed for the orange photoluminescence. All these measurements clearly show that prolonged UV irradiation only affects the manganese emitting centers and not at all the structural blende-lattice defects, making the hypothesis of passivation of surface defects as a possible origin of the observed emission-intensity increase questionable.

So, to tentatively understand the origin of the luminescence growth mechanism in our particles during UV irradiation, we have performed a series of structural characterizations, focusing first on their surface and then on their manganese centers. To this aim, we have analyzed them before and after irradiation by XPS and FTIR techniques, as shown in Fig. 6. Both characterizations clearly show an oxidation of surface sulphide ions S^{2-} intro sulfate ones SO_4^{2-}. Indeed, the FTIR spectrum of the irradiated particles exhibits three absorption peaks at 1120, 980 and 620 cm^{-1}, corresponding to the asymmetric stretch ν_3, symmetric stretch ν_1 and asymmetric bend ν_4 vibrations of sulfates. [46] These bands are much weaker in the fresh particle spectrum (Fig. 6a). Moreover, the S_{2p} XPS spectrum of the irradiated exhibits two signatures (Fig. 6b), those of S^{2-} and SO_4^{2-} characteristic peaks at ~162 and ~169 eV, respectively [47]. Only the peak centered at ~162 eV is observable in the spectrum collected on fresh particles (Fig. 6b). An attentive reading of the bending energy of the S^{2-} peak evidences a small intensity decrease and energy position increase. Such a feature was already reported on UV-irradiated manganese-doped ZnS nanoparticles along several hours (2 and 6 hours) and was attributed to the formation of a thin sulfate outer layer. In that case, the intensity-peak decrease reached 30% and 56% while the average bending energy shift reached 0.2 and 0.5 eV, respectively [48]. Within our exposition conditions these effects are less obvious, buy still clearly present.

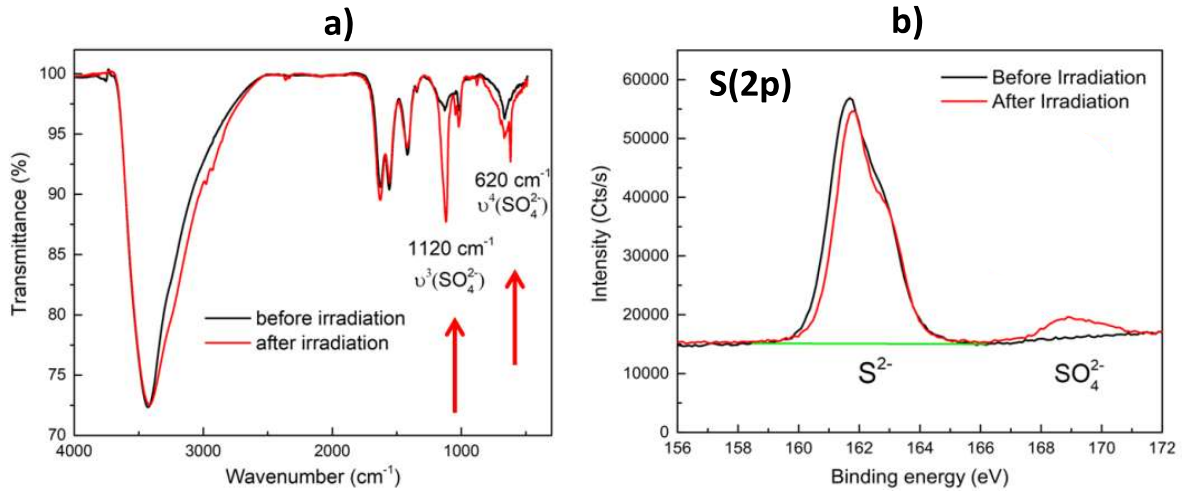

Figure 6. a) FTIR and b) S(2p) XPS spectra of the particles recorded before (black line) and after 30 min of UV irradiation (red line). XPS peak fitting was performed on the whole S_{2p} signal and the deconvoluted lines are plotted n Fig. S2 in the supporting information section.

To evidence this outer metal sulfate layer, we performed TEM and XRD analysis on the irradiated particles. In the first case, the UV-exposed (over 30 minutes) ethanolic colloidal dispersion was deposited on a TEM grid for observation, while in the second case the same suspension was spin-coated on a ITO/glass substrate (see experimental section) and its grazing incidence X-ray diffraction (GIXRD) pattern was recorded and compared to that of the film prepared from a fresh colloidal suspension. The smallness of the studied particles makes the evidence of any structural change hard to observe by TEM. The recorded

micrographs at different magnifications (not shown) do not allow to identify either surface strain effect or surface segregation (see Fig. S5 in the supporting information). On the contrary, the comparison of the XRD patterns is much more conclusive (Fig. 7). Indeed, a net peak intensity decrease and line broadening increase can be observed after UV irradiation in agreement with local strains induced by blende-lattice micro-deformation and/or crystal size decrease, the former being the most probable, since TEM observation suggested great morphological proximity between the fresh and irradiated particles. Noteworthy, no significant shift towards larger angles as a consequence of uniform residual strains and/or composition changes were observed on the recorded pattern. To support these conclusions, an estimation of the thickness of the oxidized layer was achieved considering the XPS sulfide and sulfate data (see the supporting information section). A value smaller than 1 Å was obtained, meaning that the sulfate layer is discontinuous and thin, making its evidence by HR-TEM observation impossible.

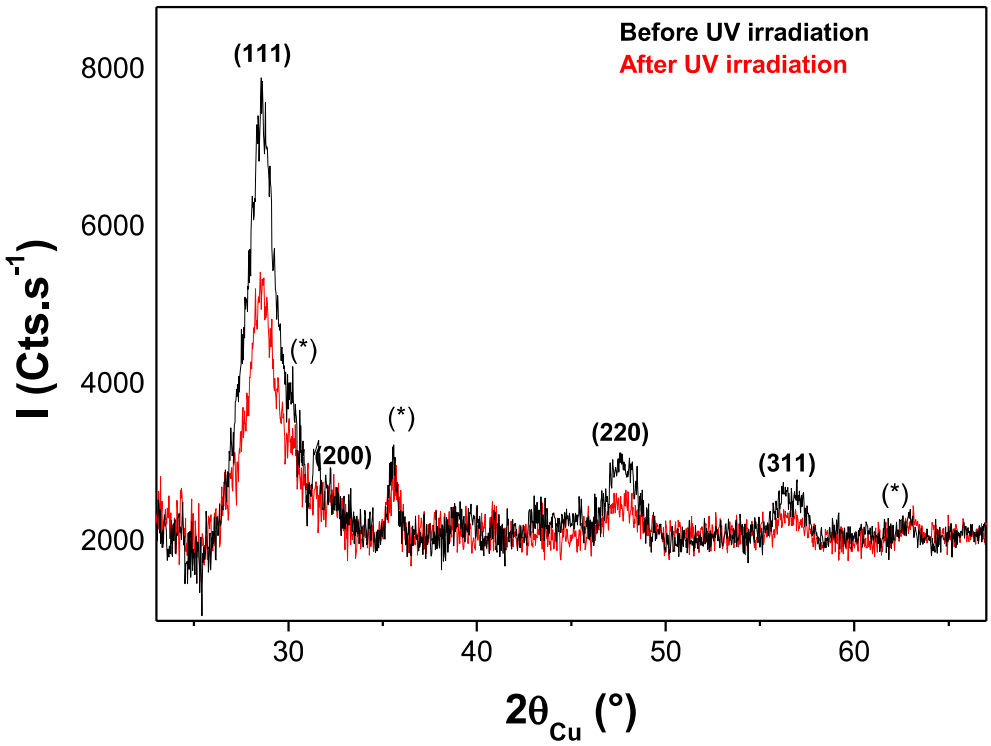

Figure 7. XRD patterns of fresh (black line) and exposed over 30 min to UV light of 305 nm in wavelength (red line) ZnS:Mn films. (*) correspond to the diffraction of the ITO substrate.

	$2\theta_{(111)}$ (deg)	Area ($Cts.s^{-1}.deg$)	Height ($Cts.s^{-1}$)	β (deg)
Before irradiation	28.531(5)	8144.06	3348	2.43
After irradiation	28.552(°	5263.57	1959	2.68

Table 1. Main diffraction peak profile parameters inferred from the XRD pattern analysis of the fresh and exposed over 30 min to UV light of 305 nm in wavelength ZnS:Mn films. Refinements were performed assuming pseudo-Voigt function, of the (111) blende phase and allowing us to highlight a peak broadening after UV exposition through the peak integral width line β increase.

To go further on this local strain effect, the ZnS:Mn powder and films, fresh and irradiated over 30 min (see the experimental section) were characterized using *ex situ* EPR spectrometry (Fig. 8a). In principle, EPR allows to detect small changes in the bonding configuration (oxidation state, symmetry…) of Mn^{2+} ions from their spin Hamiltonian parameters.
From the results obtained with the sample before irradiation, we already stress a predictable difference between the obtained EPR spectra and the one corresponding to an ideal sample in which the manganese ions do not interact with each other. As a matter of fact, the dipole-dipole interaction between these ions is responsible for the broad Lorentzian-like background that we observe in the EPR spectra (Fig. 8a) before irradiation. Both spectra share the well-known splitting of the signal into a sextet of peaks, due to hyperfine interaction [49]. Nevertheless, two main differences between the EPR spectra before and after irradiation need to be emphasized. First, the shape of the 6 bands is slightly modified as a result of irradiation, being more peaked (see Fig. 8b). Moreover, the two peaks external to the sextet region are shifted and enlarged.

In order to quantitatively evaluate the impact of UV irradiation on the sample, we have realized a theoretical simulation after subtracting a fitted Lorentzian background from both spectra. The theoretical model is based on a Hamiltonian including a Zeeman term, which represents the interaction of each individual spin S with the external magnetic field B, a hyperfine term, which traduces the interaction between the nuclear spin I and the electron spin S, and a zero-field splitting term, that removes the degeneracy of the $2S+1$ manifold in zero magnetic field, which becomes relevant for ions with spin $S > ½$ in ligand symmetries lower than octahedral. The values D and E/D parameterize the axial and rhombic symmetry of the metal center: [50]

$$\mathrm{H} = \beta g \vec{\mathrm{S}}.\vec{\mathrm{B}} + A\vec{\mathrm{S}}.\vec{\mathrm{I}} + D\left[S_z^2 - \frac{S}{3}(S+1) + \frac{E}{D}(S_x^2 - S_y^2)\right] \qquad \text{Eq. 5}$$

The fitting was performed assuming the following hypotheses: 1) the hyperfine tensor A is replaced by the hyperfine constant A (isotropic system) and 2) the rhombohedral parameter E is neglected (only axial symmetry around the metal center).
For the two spectra, before and after irradiation, the resulting fitting function included the Landé factor parameter g, which was found to be equal to 2.0067 ± 0.0020. This value is slightly higher than that reported for bulk cubic ZnS:Mn (g = 2.0022 [51]) but still consistent with Mn^{2+} cation within a blende structure. The discrepancy between the two values can be indeed explained as a quantum confinement effect [52–55]. The value of the parameter A, accounting for the hyperfine splitting, was found to be 190 MHz for both spectra (see Table 1). The last relevant fitting parameter was D, which specifies the Zero Field Splitting. For a manganese ion located in an ideal undistorted tetrahedral site the D value should be zero,

resulting in an EPR spectrum showing only the already mentioned splitting into six lines. Experimentally, it is never equal to zero for any nanosized real sample [56,57], but its size quantifies the degree of local constraint experienced by the metal ions.

We stress that the NPs in the powder are expected to display a distribution of size, shape as well as of number, position and type of defects in the crystalline structure. Moreover, also within each single NP, the local environment of every Mn site can vary as a result of its position.

This heterogeneity in the sample was already highlighted when we discussed the physical meaning of the time dependence of the phosphorescence decay. In order to take into account all these effects, a Gaussian distribution of the *D* parameter has been introduced, and its Full Width Half Maximum (FWHM) has been used as an additional parameter of the fitting procedure. Values of 160 and 50 MHz were thus found for *D* and FWHM before irradiation, and values of 210 and 75 MHz respectively, after irradiation (see Table 1 and Figs. 8c and 8d).

	***A* parameter (MHz)**	**Average value of *D* (MHz)**	**FWHM of *D* (MHz)**
Before irradiation	190	160	50
After irradiation	190	210	75

Table 2. Average values of the *A* parameter (see Eq. 5) and of the average and FWHM of the Gaussian distribution of the *D* parameter obtained from the fitting procedure, before and after irradiation.

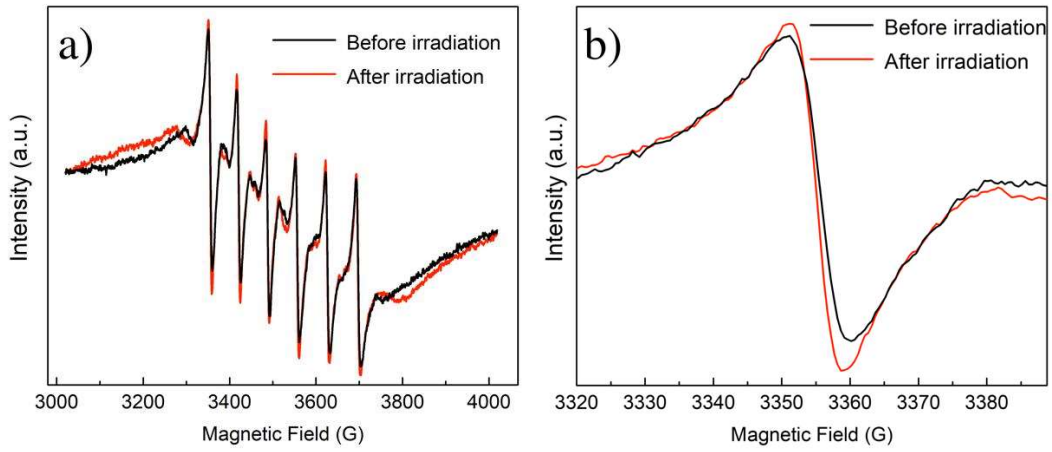

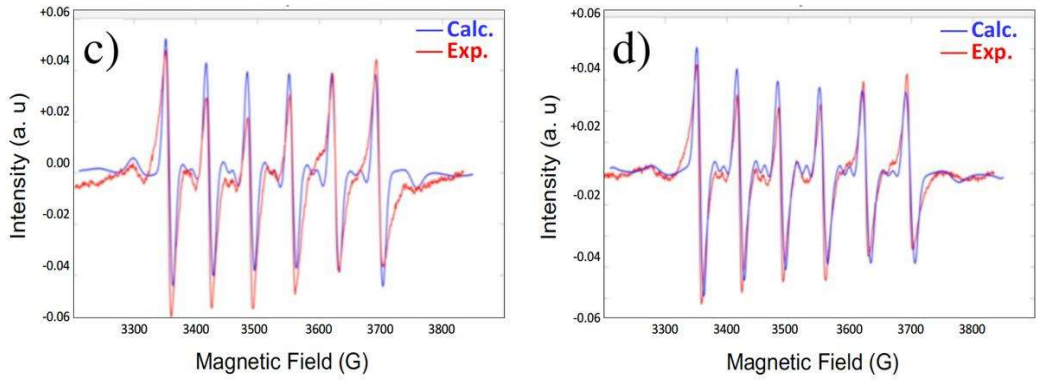

Figure 8. a) EPR spectra collected on the composite powder before (black line) and after (red line) 30 min UV irradiation. b) Enlarged view of the first peak. (c)-(d) Superposition of the calculated and experimental spectra (after dipolar contribution subtraction) c) before and d) after irradiation.

Therefore, EPR data show an increase of zero-field splitting induced by UV irradiation, suggesting an increased local distortion around the Mn^{2+} site in the irradiated ZnS:Mn NP. As stated above, the d-d transition between states $^6A_1$ and $^4T_1$ violates both the spin selection rule $\Delta S = 0$ and the Laporte rule. As already discussed, both are actually lifted for a Mn ion in a tetrahedral ZnS lattice, the former as a result of spin-orbit coupling, the latter by the presence of a hybridization of p and d orbitals due to the absence of an inversion center in a tetrahedral configuration. In other words, the lower symmetry of the system compared, for example, to an octahedral configuration, increases the transition probability between these two states. The distortion we invoke as a result of UV irradiation does not affect, to a first approximation, the spin properties of the system. On the contrary, it is reasonable to assume that it induces a further reduction of the degree of symmetry of the system, pushing further the orbital p-d hybridization (increasing the p character), and thus increasing the transition probability. More specifically, our quantitative EPR analysis neglecting the parameter *E* is compatible with a distortion of the Mn tetrahedral site along a trigonal axis. According to the character tables of group theory, in the Td geometry, only three d orbitals exhibit the same behavior toward symmetry operations as the three p orbitals, while this number increases after a compression along a C_3 axis (the most probable) or after an elongation, as illustrated in the character table of the C_{3v} symmetry group [58].

CONCLUSIONS

We have highlighted an increased orange emission of Manganese-doped ZnS NPs due to irradiation with UV light. The absence of modification of the blue emission clearly suggests that a passivation effect is excluded. As a matter of fact, passivation usually occurs when a surface treatment removes surface trapping defects that are usually at the origin of non-radiative decay paths. Since, as already pointed out, in our experiment all the observed emitting paths are excited only through a band-to-band excitation, passivation should affect all the possible radiative paths in a non-selective way, coherently with previous results, for which both blue and orange emission were modified, the intensity increase of the former

being stronger [19,20]. Our interpretation, corroborated by an EPR study before and after irradiation, ascribes this enhancement to a local modification of the environment around Mn^{2+} ions in each NP. This increased strain is due the creation of sulfate ions, independently confirmed by XPS and FTIR measurements. As a consequence of this strain, the symmetry of Mn sites is reduced, so that a higher degree of p-d hybridization stems from it, resulting in an increased transition probability.

These results are important because they highlight the non-trivial role of local strains on the manganese phosphorescence, since they may further lift the orbital selection rules controlling the electronic transition of $[MnS_4]^{6-}$ center, and point out the minor role of passivation phenomenon on the phosphorescence enhancement.

AUTHOR INFORMATION

Corresponding Authors

*Address: 15 Rue Jean-Antoine de Baïf 75205, Paris cedex 13, France. E-Mail addresses : antonio.longo@univ-paris-diderot.fr, ammarmer@univ-paris-diderot.fr,

SUPPORTING INFORMATION

The supporting information section contains the chemical mapping of TEM imagines of our samples, the tauc plot along with an estimate of the energy bandgap, the decay kinetics of the emission bands peaking at 310 and 410 nm, some pictures under UV light of substrates covered with NPs before and after irradiation, and a TEM image of UV-irradiated NPs.

ACKNOWLEDGMENTS

The authors are grateful to Drs. S. Nowak and P. Decorsec (Université de Paris) for their respective technical assistance during XRD, XRF and XPS experiments. This work was supported by the French Ministry of Research. ANR (*Agence Nationale de la Recherche*) and CGI (*Commissariat à l'Investissement d'Avenir*) are gratefully acknowledged for their financial support of this work through Labex SEAM (ANR-11-LABX-086, ANR-11-IDEX-0502) grant. It obtained also a financial support for its operating cost from ACTINOVA Company.

REFERENCES

1. Wang, Y.; Herron, N. Nanometer-sized semiconductor clusters: materials synthesis, quantum size effects, and photophysical properties. *J. Phys. Chem.* **1991**, *95*, 525-532.

2. Chen, W.; Wang, Z.; Lin, Z.; Lin, L. Absorption and luminescence of the surface states in ZnS nanoparticles. *Journal of Applied Physics* **1997**, *82*, 3111-3115.
3. Jahanbin, T.; Gaceur, M.; Gros-Dagnac, H.; Benderbous, S.; Ammar, S. A. High potential of Mn-doped ZnS nanoparticles with different dopant concentrations as novel MRI contrast agents: synthesis and in vitro relaxivity studies. *J. Nanopart. Res.* **2015**, *17*, 258.
4. Gaceur, M.; Giraud, M.; Hemadi, M.; Nowak, S.; Menguy, N.; Quisefit, J.-P.; David, K.; Jahanbin, T.; Benderbous, S.; Boissière, M.; Ammar, S. Polyol-synthesized $Zn_{0.9}Mn_{0.1}S$ nanoparticles as potential luminescent and magnetic bimodal imaging probes: Synthesis, characterization, and toxicity study. *J. Nanopart. Res.* **2012**, *14*, 932.
5. Xu, C. N.; Watanabe, T.; Akiyama, M.; Zheng, X. G. Preparation and characteristics of highly triboluminescent ZnS film. *Mater. Res. Bull.* **1999**, *34*, 1491-1500.
6. Prevenslik, T. V. Acoustoluminescence and sonoluminescence. *J. Luminescence* **2000**, *87–89*, 1210-1212.
7. Biswas, S.; Kar, S.; Chaudhuri, S. Optical and magnetic properties of manganese-incorporated zinc sulfide nanorods synthesized by a solvothermal process. *J. Phys. Chem. B* **2005**, *109*, 17526-17530.
8. Datta, A.; Biswas, S.; Kar, S.; Chaudhuri, S. Multicolor luminescence from transition metal ion (Mn^{2+} and Cu^{2+}) doped ZnS nanoparticles. *J. Nanosci. Nanotechnol.* **2007**, *7*, 3670-3676.
9. Mishra, P.; Ojha, K. S.; Khare, A. Structural and optical study of copper-doped zinc sulfide nanoparticles. *J. Appl. Spectrosc.* **2018**, *85*, 743-748.
10. Manzoor, K.; Vadera, S. R.; Kumar, N.; Kutty, T. R. N. Multicolor electroluminescent devices using doped ZnS nanocrystals. *Appl. Phys. Lett.* **2004**, *84*, 284-286.
11. Mei, S.; Zhang, G.; Yang, W.; Wei, X.; Zhang, W.; Zhu, J.; Guo, R. A facile route for highly efficient color-tunable Cu-Ga-Se/ZnSe quantum dots. *Appl. Surf. Sci.* **2018**, *456*, 876-881.

12. Wei, X.; Mei, S.; Zhang, G.; Su, D.; Xie, F.; Zhang, W.; Guo, R. Enhanced tunable dual emission of Cu:InP/ZnS quantum dots enabled by introducing Ag ions. *Appl. Surf. Sci.* **2019**, *493*, 605-612.

13. Bhargava, R. N.; Gallagher, D.; Hong, X.; Nurmikko, A. Optical properties of manganese-doped nanocrystals of ZnS. *Phys. Rev. Lett.* **1994**, *72*, 416-419.
14. Chung, J. H.; Ah, C. S.; Jang, D.-J. Formation and distinctive decay times of surface- and lattice-bound Mn^{2+} impurity luminescence in ZnS nanoparticles. *J. Phys. Chem. B* **2001**, *105*, 4128-4132.
15. Xu, S. J.; Chua, S. J.; Liu, B.; Gan, L. M.; Chew, C. H.; Xu, G. Q. Luminescence characteristics of impurities-activated ZnS nanocrystals prepared in microemulsion with hydrothermal treatment. *Appl. Phys. Lett.* **1998**, *73*, 478-480.
16. Murugadoss, G. Synthesis of ZnS:Mn^{2+} and ZnS:Mn^{2+}/ZnS core–shell nanoparticles using poly(methyl methacrylate). *Appl. Nanosci.* **2013**, *3*, 485-493.
17. Wang, S.; Jarrett, B. R.; Kauzlarich, S. M.; Louie, A. Y. Core/shell quantum dots with high relaxivity and photoluminescence for multimodality imaging. *J. Am. Chem. Soc.* **2007**, *129*, 3848-3856.
18. Quan, Z.; Wang, Z.; Yang, P.; Lin, J.; Fang, J. Synthesis and characterization of high-quality ZnS, ZnS:Mn^{2+}, and ZnS:Mn^{2+}/ZnS (core/shell) luminescent nanocrystals. *Inorg. Chem.* **2007**, *46*, 1354-1360.

19. Bol, A. A.; Meijerink, A. Luminescence quantum efficiency of nanocrystalline ZnS:Mn^{2+} 2: enhancement by UV irradiation. *J. Phys. Chem. B* **2001**, *105*, 10203-10209.
20. Bol, A. A.; Meijerink, A. Luminescence Quantum efficiency of nanocrystalline ZnS:Mn^{2+} 1: surface passivation and Mn $^{2+}$ concentration. *J. Phys. Chem. B* **2001**, *105*, 10197-10202.
21. Cruz, A. B.; Shen, Q.; Toyoda, T. Studies on the effect of UV irradiation on Mn-doped ZnS nanoparticles. *Materials Science and Engineering: C* **2005**, *25*, 761-765.
22. Briones Cruz, A.; Shen, Q.; Toyoda, T. The effect of ultraviolet irradiation on the photothermal, photoluminescence and photoluminescence excitation spectra of Mn-doped ZnS nanoparticles. *Thin Solid Films* **2006**, *499*, 104-109.
23. Cao, L.; Zhang, J.; Ren, S.; Huang, S. Luminescence enhancement of core-shell ZnS:Mn/ZnS nanoparticles. *Appl. Phys. Lett.* **2002**, *80*, 4300-4302.
24. Thai, D. V.; Thi, T. M.; Ben, P. V.; Lap, D. V.; Uyen, N. T.; Thu, H. H. The effect of ultraviolet irradiation on the optical properties of ZnS: Mn synthesized by hydrothermal method and using thioglycolic acid. in *2014 Conference on Optoelectronic and Microelectronic Mater. Devices* **2014**, 117-120.
25. Dunstan, D. E.; Hagfeldt, A.; Almgren, M.; Siegbahn, H. O. G.; Mukhtar, E. Importance of surface reactions in the photochemistry of zinc sulfide colloids. *J. Phys. Chem.* **1990**, *94*, 6797-6804.
26. Jung, D.-R.; Kim, J.; Park, B. Surface-passivation effects on the photoluminescence enhancement in ZnS:Mn nanoparticles by ultraviolet irradiation with oxygen bubbling. *Appl. Phys. Lett.* **2010**, *96*, 211908.
27. Torimoto, T.; Adachi, T.; Okazaki, K. I.; Sakuraoka, M.; Shibayama, T.; Ohtani, B.; Kudo, A.; Kuwabata, S. Facile synthesis of ZnS-$AgInS_2$ solid solution nanoparticles for a color-adjustable luminophore, *J. Am. Chem. Soc.* **2007**, *129*, 12388-12389.
28. Cichy, B.; Wawrzynczyk, D.; Samoc, M.; Stręk, W. Electronic properties and third-order optical nonlinearities in tetragonal chalcopyrite $AgInS_2$, $AgInS_2$/ZnS and cubic spinel $AgIn_5S_8$, $AgIn_5S_8$/ZnS quantum dots, *J. Mater. Chem. C* **2017**, *5*, 149-158.
29. Mei, S. Zhu, J.; Yang, W.; Wei, X.; Zhang, W.; Chen, Q.; He, L.; Jiang, Y.; Guo, R. Tunable emission and morphology control of the Cu-In-S/ZnS quantum dots with dual stabilizer via microwave-assisted aqueous synthesis. *J. Alloy and Compounds* **2017**, *729*, 1-8.

30. Su, D.; Wang, L.; Li, M.; Mei, S.; Wei, X.; Dai, H.; Hu, Z.; Xie, F.; Guo, R. Highly luminescent water-soluble AgInS2/ZnS quantum dots-hydrogel composites for warm white LEDs. *J. Alloy and Compounds* **2020**, *824*, 153896.

31. Grau, J.; Akinc, M. Synthesis of nickel sulfide powders by thioacetamide in the presence of urea. *J. Am. Ceram. Soc.* **1997**, *80*, 941-951.
32. Abza, T.; Ampong, F. K.; Hone, F. G.; Nkrumah, I. A new route for the synthesis of CdS thin films from acidic chemical baths. *Int. J. Thin Fil. Sci. Tec.* **2017**, *6*, 67-71.
33. Gharabaghi, M.; Irannajad, M.; Azadmehr, A. R. Selective sulphide precipitation of heavy metals from acidic polymetallic aqueous solution by thioacetamide. *Ind. Eng. Chem. Res.* **2012**, *51*, 954-963.
34. Cao, J.; Zhang, G.; Mao, Z.; Fang, Z.; Yang, C. Precipitation of valuable metals from bioleaching solution by biogenic sulfides. *Miner. Eng.* **2009**, *22*, 289-295.
35. Manaia, E. B.; Berbel Manaia, E.; Kiatkoski Kaminski, R. C.; Caetano, B. L.; Magnani, M.; Meneau, F.; Rochet, A.; Santilli, C. V.; Briois, V.; Bourgaux, C.; Chiavacci, L. A.

The critical role of thioacetamide concentration in the formation of ZnO/ZnS heterostructures by sol-gel process. *Nanomaterials* **2018**, *8*, 55.
36. Gaur, R.; Jeevanandam, P. PbS micro-nanostructures with controlled morphologies by a novel thermal decomposition approach. *J Nanopart Res* **2016**, *18*, 80.
37. Sahai, S.; Husain, M.; Shanker, V.; Singh, N.; Haranath, D. Facile synthesis and step by step enhancement of blue photoluminescence from Ag-doped ZnS quantum dots. *J. Colloid Interface Sci.* **2011**, *357*, 379-383.
38. Meyers, M. A.; Mishra, A.; Benson, D. J. Mechanical properties of nanocrystalline materials. *Prog. Mater. Sci.* **2006**, *51*, 427-556.
39. Wang, G.; Huang, B.; Li, Z.; Lou, Z.; Wang, Z.; Dai, Y.; Whangbo, M.-H. Synthesis and characterization of ZnS with controlled amount of S vacancies for photocatalytic H_2 production under visible light. *Sci. Rep.* **2015**, *5*, 8544.
40. Chaguetmi, S.; Mammeri, F.; Nowak, S.; Decorse, P.; Lecoq, H.; Gaceur, M.; Ben Naceur, J.; Achour, S.; Chtourou, R.; Ammar, S. Photocatalytic activity of TiO_2 nanofibers sensitized with ZnS quantum dots. *RSC Adv.* **2013**, *3*, 2572-2580.
41. Dengo, N.; Vittadini, A.; Natile, M. M.; Gross, S. In-depth study of ZnS nanoparticle surface properties with a combined experimental and theoretical approach. *J. Phys. Chem. C* **2020**, *124*, 7777-7789.
42. Barreca, D.; Gasparotto, A.; Maragno, C.; Tondello, E.; Spalding, T. R. Analysis of nanocrystalline ZnS thin films by XPS. *Surf. Sci. Spectra* **2002**, *9*, 54-61.
43. Nesbitt, H. W.; Banerjee, D. Interpretation of XPS Mn(2p) spectra of Mn oxyhydroxides and constraints on the mechanism of MnO_2 precipitation. *Am. Mineral.* **1998**, *83*, 305-315.
44. Ilton, E. S.; Post, J. E.; Heaney, P. J.; Ling, F. T.; Kerisit, S. N. XPS determination of Mn oxidation states in Mn (hydr)oxides. *Applied Surface Science* **2016**, *366*, 475-485.
45. Cerrato, J. M.; Hochella, M. F.; Knocke, W. R.; Dietrich, A. M.; Cromer, T. F. Use of XPS to identify the oxidation state of Mn in solid surfaces of filtration media oxide samples from drinking water treatment plants. *Environ. Sci. Technol.* **2010**, *44*, 5881-5886.
46. Lane, M. D. Mid-infrared emission spectroscopy of sulfate and sulfate-bearing minerals. *Am. Mineral.* **2007**, *92*, 1-18.
47. Chaguetmi, S.; Chaperman, L.; Nowak, S.; Schaming, D.; Lau-Truong, S.; Decorse, P.; Beaunier, P.; Costentin, C.; Mammeri, F.; Achour, S.; Ammar, S. Photoelectrochemical properties of ZnS- and CdS-TiO_2 nanostructured photocatalysts: Aqueous sulfidation as a smart route to improve catalyst stability. *J. Photochem. Photobiol. A* **2018**, *356*, 489-501.
48. Lu, S. W.; Schmidt, H. K. Photoluminescence and XPS analyses of Mn^{2+} doped ZnS nanocrystals embedded in sol–gel derived hybrid coatings. *Mater. Res. Bull.* **2008**, *43*, 583-589.
49. Kripal, R.; Gupta, A. K. EPR and optical studies of ZnS:Mn nanoparticles. **2010**, *7*, 203-209.
50. Petasis, D. T.; Hendrich, M. P. Quantitative interpretation of multifrequency multimode EPR spectra of metal containing proteins, enzymes, and biomimetic complexes. *Methods in Enzymology* **2015**, *563*, 171-208.
51. Ghica, D.; Nistor, S. V.; Nistor, L. C.; Stefan, M.; Mateescu, C. D. Structural phase transformations in annealed cubic ZnS nanocrystals. *J Nanopart Res* **2011**, *13*, 4325-4335.
52. Nistor, S. V.; Stefan, M. In-depth investigation of EPR spectra of Mn^{2+} ions in ZnS single crystals with pure cubic structure. *J. Phys.: Condens. Matter* **2009**, *21*, 145408.

53. Nistor, S. V.; Stefan, M.; Nistor, L. C.; Goovaerts, E.; van Tendeloo, G. Incorporation and localization of substitutional Mn^{2+} ions in cubic ZnS quantum dots. *Phys. Rev. B* **2010**, *81*, 035336.
54. Igarashi, T.; Ihara, M.; Kusunoki, T.; Ohno, K.; Isobe, T.; Senna, M. Characterization of Mn^{2+} coordination states in ZnS nanocrystal by EPR spectroscopy and related photoluminescence properties. *J. Nanopart. Res.* **2001**, *3*, 51-56.
55. Liu, C.; Liu, J.; Xu, W. The g factor-shift in ZnS:Mn^{2+} nanocrystals/pyrex glasses composites. *Mater. Sci. Eng. B* **2000**, *75*, 78-81.
56. Igarashi, T.; Isobe, T.; Senna, M. EPR study of Mn^{2+} electronic states for the nanosized ZnS:Mn powder modified by acrylic acid. *Phys. Rev. B* **1997**, *56*, 6444.
57. Nistor, S. V.; Stefan, M.; Nistor, L. C.; Ghica, D.; Vlaicu, I. D. Distribution and interaction of Mn^{2+} ions incorporated in cubic ZnS quantum dots over a broad concentration range. *J. All. Compds.* **2016**, *662*, 193-199.
58. Mikheykin, A. S.; Torgashev, V. I.; Yuzyuk, Yu. I.; Bush, A. A.; Talanov, V. M.; Cervellino, A.; Dmitriev, V. P. The cooperative Jahn–Teller effect and anti-isostructural phases in $Ni_{1-x}Co_xCr_2O_4$ solid solutions: Synchrotron X-ray diffraction study. *J. Phys. Chem. Solid* **2015**, *86*, 42-48.